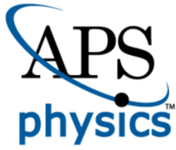

CHORUS

This is the accepted manuscript made available via CHORUS. The article has been published as:

Giant Stokes shift for charged vacancies in monolayer SnS

Anne Marie Z. Tan, Maria A. Garcia, and Richard G. Hennig

Phys. Rev. Materials **6**, 044003 — Published 11 April 2022

DOI: 10.1103/PhysRevMaterials.6.044003

Giant Stokes shift for charged vacancies in monolayer SnS

Anne Marie Z. Tan,[1, 2, 3, *] Maria A. Garcia,[2] and Richard G. Hennig[2, 3, †]

[1]School of Mechanical and Aerospace Engineering, Nanyang Technological University, Singapore 639798, Singapore
[2]Department of Materials Science and Engineering, University of Florida, Gainesville, FL 32611, USA
[3]Quantum Theory Project, University of Florida, Gainesville, FL 32611, USA

(Dated: March 18, 2022)

We perform first-principles density functional theory calculations to determine the equilibrium defect structures, formation energies, charge transition levels, and electronic structures of Sn and S vacancies in monolayer SnS. Both Sn and S vacancies exhibit multiple charge transition levels and in-gap defect states, indicating that they may be stable in different charge states depending on the Fermi level in the system. Depending on the charge state of the vacancy, the easily-distorted SnS lattice undergoes different relaxations, and in some cases, symmetry-breaking reconstructions, creating defect states within the gap that electrons can occupy at a lower energetic cost. Due to significant atomic relaxations between the equilibrium defect structures in different charge states, optical charge transitions involving both types of vacancies exhibit significant Stokes shifts of over 1 eV, which may provide opportunities for increased efficiency in light emission diode, solar cell, and solar concentrator applications.

I. INTRODUCTION

Layered bulk SnS (herzenbergite) has been studied as a potential thin-film photovoltaic absorber because of its indirect bandgap of 1.1 eV (similar to silicon) and high optical absorption coefficients [1]. More recently, single-layered SnS has also attracted interest due to its unique properties, many of which derive from its corrugated orthorhombic structure. While most of the widely-studied 2D materials (graphene, transition metal dichalcogenides, e.g., MoS_2) are hexagonal, 2D SnS is isoelectronic to phosphorene and has an analogous rectangular crystal structure. However, due to the two different atomic species, the symmetry of the crystal is reduced, leading to a more distorted puckered structure shown in Fig. 1, which gives rise to a strong piezoelectric and ferroelectric response. Strong intrinsic piezoelectricity has been predicted [2] and recently experimentally measured [3] in monolayer SnS, suggesting possible applications as piezoelectric nanogenerators. Monolayer group-IV monochalcogenides have been predicted to be multiferroic with coupled ferroelectricity and ferroelasticity and low switching barriers, which suggest potential applications in nonvolatile memory, sensors, and nonlinear optoelectronics [4]. Recently, purely in-plane room temperature ferroelectricity has been demonstrated in monolayer SnS [5], in contrast to the more commonly reported out-of-plane ferroelectricity in other 2D materials. 2D SnS may also have applications for spintronics and valleytronics applications due to the unique band structure, which has two pairs of valleys that can be separately excited with linearly polarized light [6].

While monolayer SnS is predicted to be energetically stable [7, 8], the synthesis of high-quality monolayers via exfoliation has been challenging due to the strong interlayer interactions between the lone-pair electrons of Sn, which are much stronger than the typical inter-layer van der Waals forces [9].

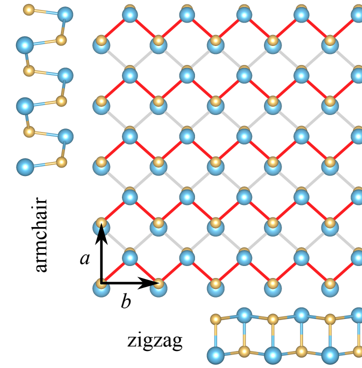

FIG. 1. Top and side views of the pristine monolayer SnS structure. Sn atoms are depicted in blue and S atoms in orange. In the top view, the Sn-S bonds are colored differently based on whether they are in the top layer (red bonds) or bottom layer (grey bonds). The *a* and *b* lattice vectors of the rectangular unit cell are also indicated.

Within the last few years, few-layer to single-layer SnS has been synthesized via techniques such as physical vapor transport [10], physical vapor deposition [5, 11], chemical vapor deposition [12], and liquid exfoliation [13]. Most recently, Khan *et al.* demonstrated a liquid metal-based technique to synthesize large-area single-crystal monolayer SnS [3]. These and other recent synthesis and characterization efforts for 2D SnS underscore the great interest in this material and its unique properties, which could have potential applications in areas including electronics, optoelectronics, non-volatile memory, and nanosensors.

Like in their bulk counterparts, 2D semiconductors contain both intrinsic defects, e.g., vacancies and antisites, as well as extrinsic defects, e.g., substitutional and interstitial dopants and impurities, all of which can affect the material's electronic, optical, and magnetic properties. In contrast to bulk materials, the reduced electronic and elastic screening of point defects in 2D materials can lead to significant changes in the charge transition levels and enhanced symmetry-breaking defect reconstructions, resulting in increased Stokes shifts. De-

* annemarie.tan@ntu.edu.sg
† rhennig@ufl.edu

fects in 2D materials that exhibit large Stokes shift open the opportunity to enhance the efficiency in energy technologies such as light emission diodes, solar cells, and solar concentrators [14–16].

Therefore, a good fundamental understanding of the effect of defects, dopants, and impurities on the properties of 2D SnS is crucial to identify and realize its potential for the aforementioned novel applications. Density functional theory (DFT) calculations have emerged as a valuable tool for predicting and characterizing point defects in solids [17], and more recently, in 2D materials as well. DFT studies on defects in layered bulk SnS predict Sn and S vacancies as well as the Sn on S antisite to be the most stable intrinsic defects with in-gap defect states [1, 18–20]. However, under much of the Sn-rich, *p*-type conditions for which Sn_S is most favorable, both Sn_S and V_S have negative formation energies, indicating a possible instability of bulk SnS. Since the vacancies are the dominant defects in bulk SnS under most conditions, and are expected to also dominate in the monolayer, therefore we focus on the vacancies in this study. Furthermore, the intrinsic *p*-type conductivity in bulk and thin film SnS has been attributed to Sn vacancies [1, 10, 18], while the presence of S vacancies has been predicted to affect the absorption of various toxic gas molecules on SnS monolayers used as a potential material for gas absorbent and sensing applications [21]. DFT studies of vacancies, dopants, or surface adsorbates in monolayer SnS have been reported [22–24]; however, all of these studies focused on characterizing only neutral defects, even though many defects in layered bulk SnS have been predicted to be stable in charge states ranging from +4 to −4 [18, 19].

In this work, we perform DFT calculations to determine the equilibrium defect structures, formation energies, charge transition levels, and electronic structures of charged Sn and S vacancies in monolayer SnS. Section II describes our computational approach and provides the details of our DFT calculations, including the charge correction scheme, which we use to ensure the correct electrostatic boundary conditions for charged defects in 2D materials. Section III presents our results first for the pristine SnS monolayer, followed by the defect energetics and electronic structures. We predict that both Sn and S vacancies have multiple charge transition levels which fall within the bandgap, indicating that they can be stable in different charge states depending on the Fermi level in the system. We find that the equilibrium defect structure depends on the defect's charge state, and due to the "floppiness" of the SnS structure, the lattice can distort significantly around the defects, at times breaking symmetry. Atomic reconstructions, which modify the bonding structure, help stabilize the defects by creating lower-energy defect states in the gap, which additional electrons can occupy at a lower energetic cost. We compare our results with defects in other 2D semiconductors and layered SnS, and discuss possible implications of the giant predicted Stokes shifts in Section IV.

II. COMPUTATIONAL DETAILS

We perform all our calculations of pristine and defected monolayer SnS using density functional theory (DFT) as implemented in the plane-wave code VASP [25]. We use projector-augmented wave potentials [26, 27] with valence electron configurations of $4d^{10}5s^25p^2$ and $3s^23p^4$ to model Sn and S, respectively. We treat the exchange-correlation using three different sets of functionals – the Perdew-Burke-Ernzerhof (PBE) [28] generalized gradient approximation (GGA) functional, the strongly constrained and appropriately normed (SCAN) [29] meta-GGA functional, and the hybrid HeydScuseriaErnzerhof functional HSE06 [30, 31] (only for calculations of pristine SnS properties). For the calculations with SCAN, we also include long-range van der Waals interactions via the SCAN+rVV10 functional [32]. We perform spin-polarized calculations employing a plane-wave cutoff energy of 520 eV, which ensures energy convergence to within 1 meV/atom. To converge the Brillion zone integration to similar accuracy, we use Methfessel-Paxton smearing [33] with a smearing energy width of 0.10 eV and Γ-centered Monkhorst-Pack *k*-point meshes [34]. For the structural relaxations, we use *k*-point meshes corresponding to at least 400 *k*-points per reciprocal atom in 2D. For the density of states calculations, we double the density of the *k*-point meshes in all directions and use Gaussian smearing with a reduced smearing width of 0.02 eV.

We model the defective systems by constructing $3 \times 3 \times 1$, $4 \times 4 \times 1$, and $5 \times 5 \times 1$ supercells based on the orthorhombic 4-atom unit cell, varying the amount of vacuum spacing between layers to be 10, 15, and 20 Å and removing atoms accordingly to create the vacancy defects. We perform the defect calculations using both PBE and SCAN+rVV10 functionals. We fix the supercell lattice vectors for all defect supercells to the equilibrium lattice constants for the corresponding functional (see Table I) and perform the atomic relaxations using the conjugate gradient algorithm. For some of the defects, we find that the structures in the smaller supercells relax to different structures than in the larger cells, likely due to overlap of elastic strain fields and/or shallow defect wave functions, leading to incorrect structural and electronic ground states with fractional band occupancies. Therefore, we report the defect structures, formation energies, and densities of states obtained from the largest ($5 \times 5 \times 1$) supercells, in which we believe the finite-size effects to be sufficiently minimized. In addition, we enforce integer band occupancies during our calculations to avoid unphysical electronic ground states with fractional band occupancies, which may arise due to wavefunction overlap [17].

The formation energy $E^f[X^q]$ of a point defect X with charge q is determined from DFT calculations using a supercell approach following

$$E^f[X^q] = E_{\text{tot}}[X^q] - E_{\text{tot}}[\text{pristine}] - \sum_i n_i \mu_i + qE_{\text{F}} + E_{\text{corr}}, \quad (1)$$

where $E_{\text{tot}}[X^q]$ and $E_{\text{tot}}[\text{pristine}]$ are the total DFT-derived energies of the supercell containing the defect X and the pristine supercell, respectively, n_i is the number of atoms of species i

added/removed to create the defect, μ_i is the chemical potential of the corresponding species, and E_F is the Fermi level, which serves as the chemical potential of the electron reservoir. In this work, we consider the Sn-rich/S-poor limit, for which the Sn chemical potential is referenced to the α-Sn phase, and the S chemical potential is given by μ_S(S-poor) = $\mu_{SnS} - \mu_{\alpha\text{-Sn}}$.

The final term in Eq. (1), E_{corr}, contains corrections to the formation energy necessary to account for the spurious electrostatic interactions between periodic images and the compensating background charge, which is implicitly introduced in supercell calculations using plane-wave DFT approaches to neutralize the overall supercell. Modeling charged defects in single-layer materials is particularly challenging because the uniform compensating background charge induces a quadratic potential across the vacuum, which leads to the unphysical divergence of the energy with vacuum spacing. In this work, we apply the correction scheme developed by Freysoldt and Neugebauer [35] to accurately compute the formation energies of charged Sn and S vacancies in monolayer SnS. The correction scheme employs a surrogate Gaussian charge model to estimate the energy correction required to remove the electrostatic artifacts due to the periodic boundary conditions and uniform compensating background charge, thus restoring the appropriate electrostatic boundary conditions for charged 2D systems. This correction scheme has an advantage in that it does not require any extrapolation, which can sometimes be misleading [36], and its effectiveness has been demonstrated in our previous studies of S vacancies [37] and dopants and dopant-vacancy complexes [38] in MoS_2 and for defects in phosphorene [39].

III. RESULTS

A. Pristine monolayer SnS

Table I compares properties of pristine monolayer SnS computed in this work using the PBE, SCAN+rVV10, and HSE06 exchange-correlation functionals with those reported in the literature. The crystal structure of pristine monolayer SnS as depicted in Fig. 1 has an orthorhombic unit cell, with in-plane lattice parameters a and b as listed accordingly in Table I. Our DFT-computed lattice constants at the PBE level agree well with those reported in previous studies [2, 22, 23, 40–42]. SCAN+rVV10 and HSE06 functionals predict a slight expansion of the unit cell along the longer a direction and a slight contraction along the shorter b direction compared to PBE. The armchair and zigzag side views of the crystal structure clearly show that SnS has a corrugated structure similar to the structure of isoelectronic phosphorene. Each Sn (S) atom is threefold coordinated and bonded to two S (Sn) atoms in the same layer and one S (Sn) atom in the other layer. For illustrative purposes, the Sn-S bonds in the top layer have been drawn in red, while those in the bottom layer are in grey.

SnS has an indirect bandgap with the VBM located between the Γ and X points and the CBM in between the Γ and Y points. Our PBE-computed bandgap agrees to within about 0.1 eV with those reported in previous studies [2, 22–24, 41]; however, since PBE is well known to underestimate the bandgaps of semiconductors, we also evaluated the bandgap with the SCAN+rVV10 and HSE06 exchange-correlation functionals. As expected, the bandgap increases from 1.50 eV to 1.83 eV (SCAN+rVV10) to 2.21 eV (HSE06), with most of the increase being due to the downward shift of the VBM, corresponding to an increased ionization energy. The experimental optical bandgap of monolayer SnS is reported to be about 1.4 eV [3]. Including the exciton binding energy, estimated using the Bethe-Salpeter Equation to be approximately 0.5 eV [43], suggests a fundamental bandgap of around 1.9 eV. While significantly larger than the bandgap calculated using PBE, this value is close to that calculated using SCAN+rVV10. Hence, we believe that the SCAN+rVV10 functional should provide quantitatively meaningful results, and moving forward, we will primarily focus on the energetics and electronic structure computed using the SCAN+rVV10 functional.

A key input to the Freysoldt-Neugebauer charge correction scheme is the dielectric profile of the monolayer. The surrogate model assumes an isotropic dielectric slab; while this may not strictly be valid for a monolayer, the simplified dielectric model correctly reproduces the asymptotic screening properties of the repeated slab system. We compute the static dielectric tensor – including both electronic and ionic contributions – within DFT for a system comprising the monolayer surrounded by vacuum and estimate the monolayer's averaged permittivity following the approach detailed in Refs. [37, 44].

The electronic contribution to the dielectric tensor, i.e., the high-frequency dielectric response, is only slightly anisotropic in the two in-plane directions, differing by only about 2%. However, the low-frequency dielectric response, which includes the effects of ionic relaxation, is highly anisotropic. Unlike in the hexagonal MoS_2 structure, where the ionic contribution to the dielectric response is negligible, the "floppy" nature of the rectangular SnS structure results in a large ionic contribution to the dielectric response. At the PBE level, the ionic contribution to the in-plane dielectric tensor components is $\approx 63\%$ and $\approx 74\%$ along the a and b directions, respectively, comparable to that reported for layered bulk SnS [18, 19]. The anisotropic structure of SnS leads to significantly different ionic relaxation along different directions, such that the in-plane dielectric response along the b direction is about 50% larger than that along the a direction. The ionic contribution to the out-of-plane dielectric tensor component is negligible. We had difficulty converging the calculations for the ionic contribution to the dielectric response at the SCAN and HSE06 levels. Therefore, the values for the slab-averaged permittivity reported in Table I combine the electronic contribution evaluated with SCAN or HSE06 with the ionic contribution from PBE. We believe that this approximation is sufficient since the charge correction scheme is not too sensitive to the choice of permittivity – changing the permittivity by $\pm 15\%$ changes the formation energies by less than 0.1 eV and the CTLs by less than 0.05 eV, which does not qualitatively change our results.

TABLE I. In-plane lattice constants a and b, bandgap E_{gap}, ionization energy (I. E.), electron affinity (E. A.), average permittivity ε^{slab}, and slab thickness d^{slab} for monolayer SnS evaluated using different exchange-correlation functionals.

	a (Å)	b (Å)	E_{gap} (eV)	I. E. (eV)	E. A. (eV)	ave. ε^{slab} (ε_0)	d^{slab} (Å)
PBE	4.32	4.07	1.50	4.66	3.16	49.3	5.73
	4.24 [40], 4.25 [22], 4.26 [2], 4.28 [23], 4.31 [41], 4.34 [42]	4.03 [2, 22], 4.05 [42], 4.07 [23, 40, 41]	1.37 [2], 1.4 [22–24], 1.46 [41]				
SCAN+rVV10	4.38	3.96	1.83	4.97	3.14	46.8	5.71
HSE06	4.37	3.98	2.21	5.16	2.95	45.5	5.84
			2.0 [24], 2.03 [41], 2.09 [42]				

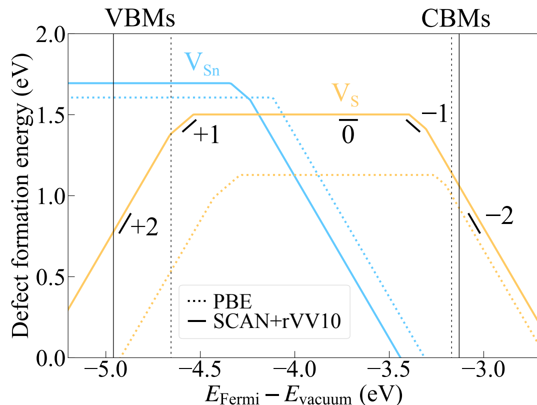

FIG. 2. Defect formation energies of the Sn vacancy (blue) and S vacancy (orange) in monolayer SnS as a function of the Fermi level, under Sn-rich/S-poor conditions, calculated with the PBE (dotted lines) and SCAN+rVV10 (solid lines) functionals. The slopes of the line segments, which correspond to the defect's stable charge state over that range of energies, are indicated on the plot. The vertical black dashed and solid lines indicate the valence and conduction band edge positions relative to the vacuum level, evaluated with each corresponding functional.

B. Defect energetics

Figure 2 shows the defect formation energies of the Sn and S vacancies in monolayer SnS as a function of the Fermi level, calculated with the PBE and SCAN+rVV10 functionals. The slopes of each line segment correspond to the most thermodynamically stable charge state of the defect over that range of energies. Therefore, the kinks in the formation energy plots indicate charge transition levels (CTLs), which correspond to the positions of defect states within the bandgap. Our calculations with the SCAN+rVV10 functional predict that the Sn vacancy may be stable in the neutral, −1, or −2 charge states and has acceptor-type $0/-1$ and $-1/-2$ CTLs, which fall within the bandgap. We note that PBE gives slightly different predictions, as it finds the −1 charged Sn vacancy to be slightly unstable. Hence only a single $0/-2$ CTL is observed in this case. However, since the singly-charged vacancy was found to be stable over only a small energy range, we still consider the PBE and SCAN+rVV10 results to be in good agreement. Meanwhile, both functionals predict that the S vacancy may be stable in charge states ranging from +2 to −2, with both donor-type $+2/+1$ and $+1/0$ CTLs and acceptor-type $0/-1$ and $-1/-2$ CTLs falling within the bandgap. The defect formation energies and CTLs predicted by both functionals are in generally good agreement with one another and qualitatively lead to the same conclusions; hence, moving forward, we only present the results computed using the SCAN+rVV10 functional.

Figure 3 compares the thermodynamic and optical CTLs for both vacancies. In Figs. 3(a) and (b), the solid lines indicate the formation energies of the defect when it is in its fully relaxed geometry for each charge state, computed using the SCAN+rVV10 functional, reproducing the result shown by the solid lines in Fig. 2 above. In addition, we have also evaluated the formation energies of the defect in configurations where the defect geometry of a different charge state has been "frozen in", which are depicted as dashed and dotted lines. This enables us to differentiate between the *thermodynamic* CTLs – in which the transition occurs slowly enough that the defect has enough time to fully equilibrate into its new ground state – and *optical* CTLs – in which the transition occurs too quickly such that the atomic geometry of the initial charge state is "frozen in" on the time scale of measurement. These CTLs are denoted as optical CTLs to indicate that such transitions typically occur during optical excitation/de-excitation processes; full consideration of optical effects – such as calculations of exciton binding effects and optical transition matrix elements – are beyond the scope of this work. The corresponding thermodynamic and optical (absorption and emission) CTLs are also represented as solid, dotted, and dashed horizontal lines in the level diagrams in Figs. 3(c) and (d).

First, let us focus on the Sn vacancy. As is evident from Figs. 3(a) and (c), the optical CTLs can differ by hundreds of meV and are not necessarily symmetric with respect to the corresponding thermodynamic CTL. For example, the $0/-1$ thermodynamic CTL occurs at −4.35 eV, while the $-1 \rightarrow 0$ optical CTL (adiabatic electron loss process) is about 0.4 eV lower in energy, while the $0 \rightarrow -1$ optical CTL (adiabatic electron capture process) is about 0.75 eV higher in energy. The large 1.15 eV difference between the optical CTLs corresponds to the Stokes shift (the energy difference between optical absorption and emission peaks), and arises because the charging/uncharging of the Sn vacancy defect in SnS is associated with large atomic relaxations. The structures of the neutral and −2 charged Sn vacancies can be seen in Figs. 4(d) and (e) (the structures of the vacancy in the −1 and −2 charged states are similar, hence only the latter is shown). The red bonds in those figures illustrate the differences in the relaxed Sn-S bonding surrounding the vacancy in the top layer of SnS. While the negatively-charged Sn vacancies relax into a sym-

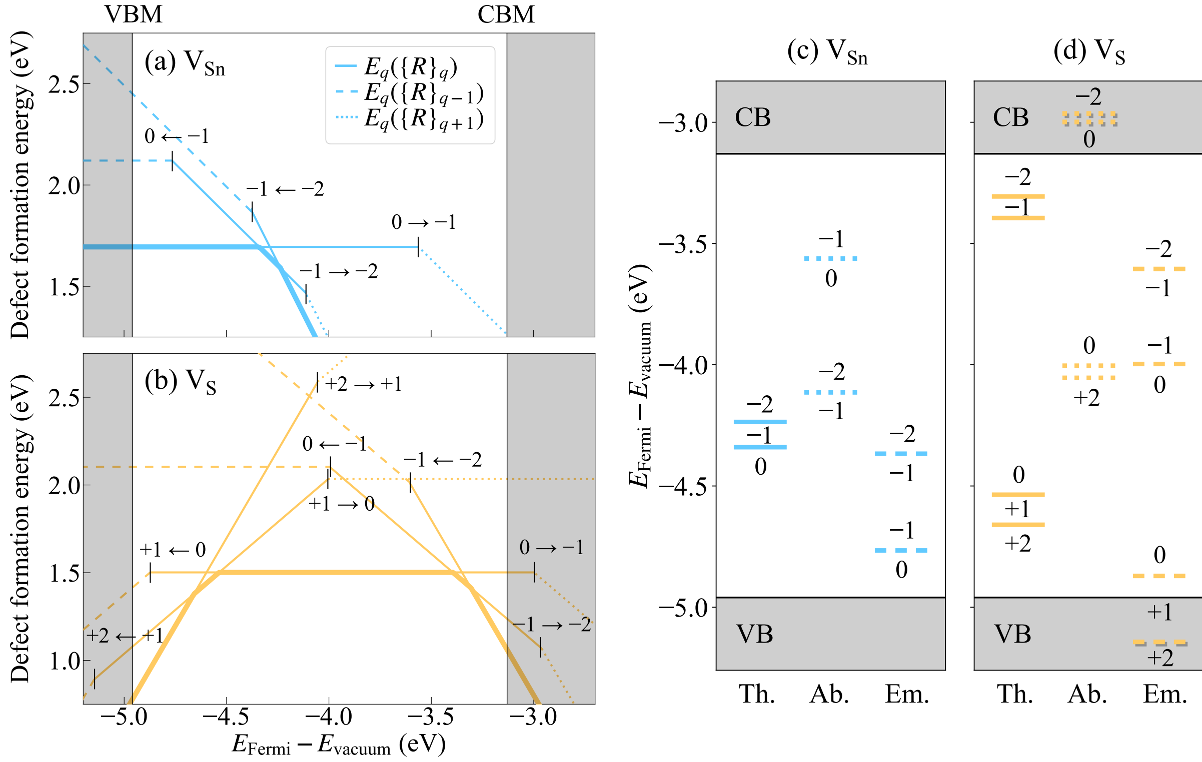

FIG. 3. Thermodynamic and optical charge transition levels for (a, c) the Sn vacancy and (b, d) the S vacancy in monolayer SnS, calculated with the SCAN+rVV10 functional. In (a) and (b), solid, dashed, and dotted lines of slope q correspond to the formation energy of the vacancy with charge q evaluated at the defect structure relaxed in the same charge state, with an additional electron, and with one fewer electron. These formation energies correspond to thermodynamic charge transition, adiabatic electron loss, and adiabatic electron capture processes, respectively. The thick bold lines indicate the most energetically favorable thermodynamic formation energy (as plotted in Fig. 2). The optical CTLs are labeled in the figure, with the arrows indicating the direction of charge transition in each case; note that these are not necessarily symmetric with respect to the corresponding thermodynamic CTL. In (c) and (d), solid, dotted, and dashed lines indicate the thermodynamic, absorption, and emission levels corresponding to the CTLs in (a) and (b).

metric configuration, the atomic relaxations around the neutral Sn vacancy are particularly interesting, as the largest distortions and "defective bonding" appear slightly away and to one side of the vacant site, at the base of the diamond-shaped bonding structure. The distorted ground state structure for the neutral Sn vacancy has not been reported in previous studies on vacancies in monolayer SnS [23, 40], perhaps due to finite size constraints on the structural relaxation, since those calculations had been performed in smaller 3×3 supercells. In our calculations utilizing 5×5 and 6×6 supercells, the distorted ground state was found to be around 350 meV lower in energy than a symmetric ground state similar to those found for the negatively-charged Sn vacancies. We note that the $-1 \rightarrow -2$ optical absorption CTL appears lower than the $0 \rightarrow -1$ optical absorption CTL due to the different electronic structures of the originating vacancy charge state: the lowest unoccupied level in the neutral vacancy is at a higher energy than that in the -1 charged vacancy (c.f. Figs. 4(a) and (b)).

Figure 3(b) shows that the S vacancy exhibits a similar behavior for the CTLs as the Sn vacancy. However, since the S vacancy may be stable in one of five charge states for energies spanning the bandgap, there are more possible CTLs to consider. To simplify the analysis, we only consider the transitions involving a single charge transfer, which should be much more likely to occur in practice. Again, the energy differences between the electron capture and electron loss optical CTLs (i.e., the Stokes shift) are on the order of hundreds of meV and can be attributed to the significant lattice relaxation energy associated with the different ground state structures of the S vacancy in different charged states (c.f. Figs. 5(d) - (i)). As we will see in the following section, the occupation of defect states by electrons favors ionic relaxations that lower the defect state's energy, hence leading to different ground state structures for different charged states.

C. Defect electronic structures

Figure 4 depicts the projected densities of states for the Sn vacancy in the neutral, -1, and -2 charge states, along with charge isosurfaces and simulated scanning tunneling microscopy (STM) images of the relevant defect orbitals. The defect densities of states are projected separately onto the s- and p-orbitals of the Sn and S atoms, while the total density

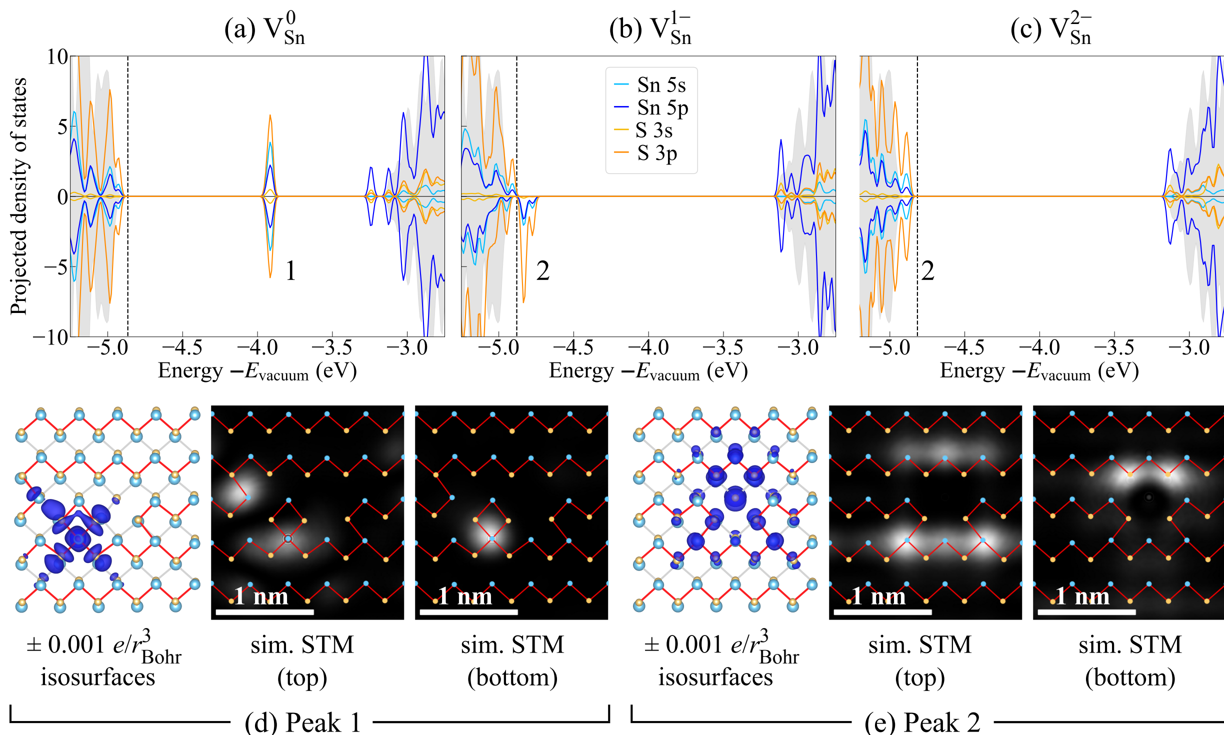

FIG. 4. Projected densities of states for the Sn vacancy in the (a) 0, (b) −1, and (c) −2 charge states, calculated with the SCAN+rVV10 functional. The densities of states are projected separately onto the s- and p-orbitals of the Sn and S atoms. For comparison, the total density of states of pristine SnS is shown in grey shading. The energies are plotted with respect to the vacuum energy, with the highest occupied level indicated by the vertical dashed line. The charge densities of the orbitals corresponding to the defect peaks marked "1" and "2" are depicted in (d) and (e). In each case, the charge density is visualized via charge isosurfaces and simulated STM images of both top and bottom surfaces. The charge densities show that the empty mid-gap defect state present in the neutral Sn vacancy is localized around a Sn atom slightly away from the defect. The white scale bar denotes a length of 1 nm.

of states of pristine monolayer SnS is shown in grey shading for comparison. We observe that the VBM is primarily made up of S 3p states, while the CBM is primarily Sn 5p states. Based on the projected densities of states, the indicated defect peaks "1" and "2" both appear to have a similar orbital character, dominated by S 3p states. However, a more detailed analysis based on the visualizations of the corresponding defect orbitals reveals that the defect states of the neutral and negatively charged Sn vacancy are, in fact, very different.

The defect orbitals corresponding to peaks "1" and "2" are shown in Figures 4(d) and (e), respectively. The orbitals are visualized via both charge isosurfaces and simulated STM images of the top and bottom surfaces of the monolayer. The Sn-S bonding structure of the top layer (where the vacancy was created) is overlaid for comparison of the atomic and electronic structures. We observe that the defect orbitals around the neutral Sn vacancy are localized around the diamond-shaped bonding structure to the left of the vacant site, breaking the lattice symmetry. Meanwhile, the defect orbitals around both −1 and −2-charged Sn vacancies are similar, preserving the lattice symmetry and remaining localized around the vacancy site. Note that although the projected densities of states and charge isosurfaces show a significant contribution from S 3p states in the defect orbitals, they tend not to show up clearly in the simulated STM images, which are dominated by the Sn orbitals as they extend further from the surfaces of the monolayer.

Figure 5 depicts the projected densities of states for the S vacancy in the +2, neutral, and −2 charge states, along with charge isosurfaces and STM images of the relevant defect orbitals. Although our calculations predict that the S vacancy may be stable in five charge states ranging from −2 to +2, since the ranges of stability for the −1 and +1 states are small, we focus here on the evenly charged states, which we believe will be more relevant in practice. As before, the defect densities of states are projected separately onto the s- and p-orbitals of the Sn and S atoms, and we identify that all the defect peaks labeled "1" to "6" are dominated by Sn 5p states.

Closer inspection of the defect orbitals once again reveals that the in-gap defect states have a noticeably different character depending on the charge state of the defect. The defect orbitals visualized via charge isosurfaces and simulated STM images are presented in Figures 5(d) – (i). Comparing the defect orbitals for the +2, neutral, and −2 charged S vacancies, it is clear that the electronic structure – as well as the atomic structure – of the vacancy changes as electrons are added to the system. Breaking the lattice symmetry creates defect states that can be occupied by electrons at lower energy,

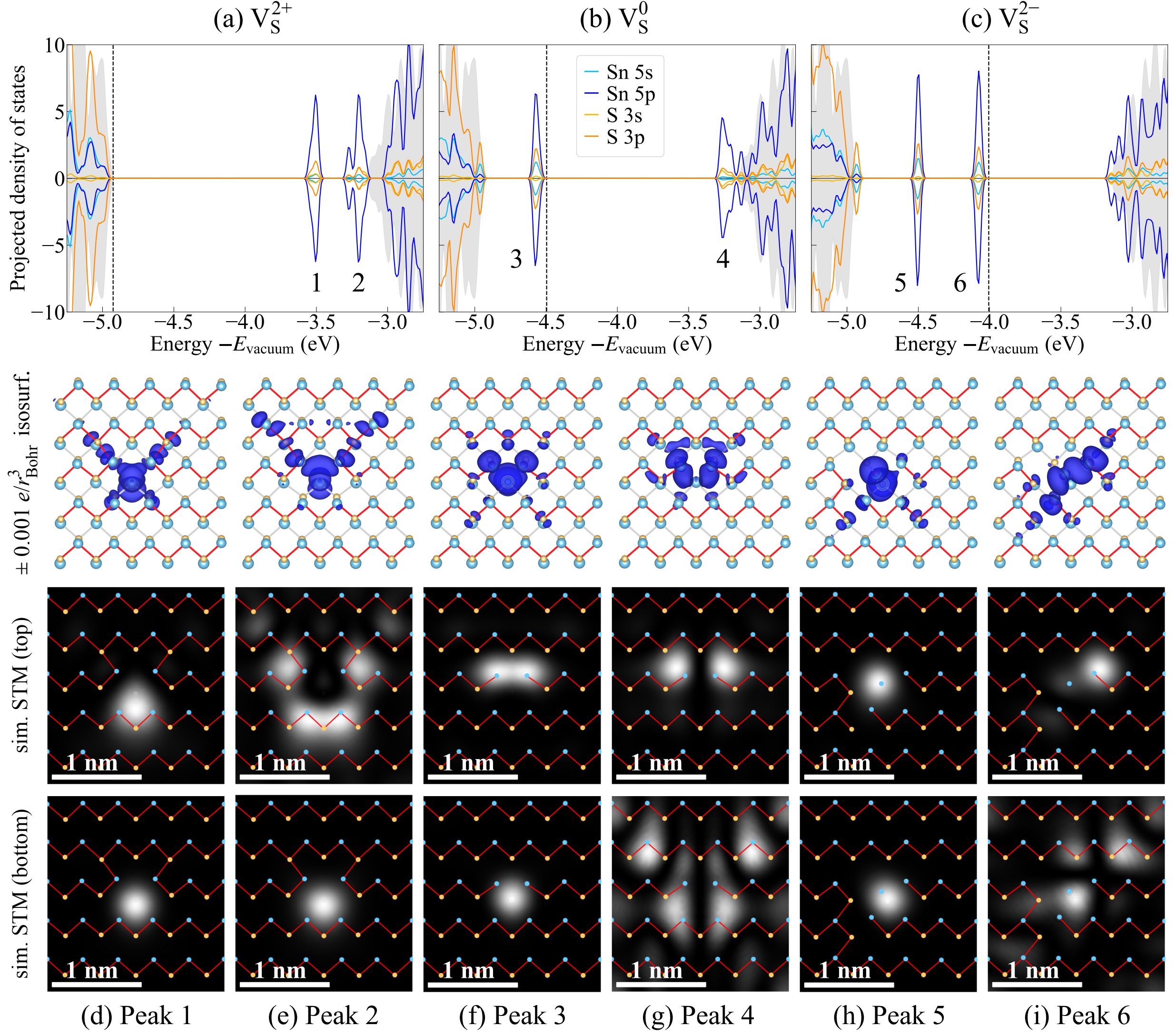

FIG. 5. Projected densities of states for the S vacancy in the (a) +2, (b) 0, and (c) −2 charge states, calculated with the SCAN+rVV10 functional. The densities of states are projected separately onto the s- and p-orbitals of the Sn and S atoms. For comparison, the total density of states of pristine SnS is shown in grey shading. The energies are plotted with respect to the vacuum energy, with the highest occupied level indicated by the vertical dashed line. The charge densities of the orbitals corresponding to the defect peaks marked "1" to "6" are depicted in (d) to (i), respectively. In each case, the charge density is visualized via charge isosurfaces and simulated STM images of both top and bottom surfaces. The charge densities show that the in-gap defect states have noticeably different character depending on the charge state of the defect, with the asymmetric orbitals reflecting the symmetry-breaking of the lattice around the negatively charged defect. The white scale bar denotes a length of 1 nm.

thus providing the driving force for structural relaxations. The simulated STM images of the defect in each charge state are distinctly unique, suggesting a means to experimentally identify and distinguish defects in different charge states in monolayer SnS.

IV. DISCUSSION

Most of the research on 2D semiconductors, their intrinsic properties, and especially studies of defects and dopants in 2D semiconductors, has focused on the transition metal dichalcogenides, which have relatively stiff lattices based on the hexagonal crystal structure. As a result, minimal atomic relaxations tend to occur around point defects such as vacancies and substitutional dopants in those 2D materials. In contrast, monolayer SnS has a relatively "floppy" corrugated orthorhombic structure that requires low energy to distort, giving this material many unique properties, including strong piezoelectric [2, 3] and ferroelectric [4, 5] response. We predict significant lattice distortions around the vacancies in monolayer SnS, which also have implications on their electronic properties and CTLs. We note that the distorted vacancy structures were not reported in previous DFT stud-

ies [23, 40], which modeled the vacancies using smaller 3×3 supercells. Indeed, we found that it was necessary to go up to larger supercell sizes of at least 5×5 to obtain the lower energy distorted structures reported in this work. This suggests that one needs to be very careful when performing calculations of defects in SnS or similar systems in which finite-size effects may preclude certain symmetry-breaking structural relaxations, leading to inaccurate prediction of ground state defect structures.

Previous studies of the NV center in diamond [45, 46] and the isoelectronic $O_N V_B$ defect in cubic boron nitride [47] determined sizable Stokes shifts of the order of 0.2 eV, which amount to less than 5% of the bandgaps in these bulk semiconductors. However, the size of the Stokes shifts in these material systems pales in comparison with our predicted Stokes shift of about 1 eV, spanning about half the size of the bandgap of 2D SnS. The larger predicted Stokes shifts in 2D SnS arise due to the considerable relaxation energies associated with the various ground-state structures of the Sn and S vacancies in different charge states, and can be attributed to the 2-dimensional orthorhombic structure of 2D SnS which allows for much larger lattice relaxations than would be possible in bulk semiconductors.

Such giant predicted Stokes shifts could have some interesting implications and potential applications. If a charge transition occurs on a time scale that does not allow complete structural relaxation, the corresponding optical CTL will be observed instead of the thermodynamic CTL. Differences in optical CTLs on the order of hundreds of meV to greater than 1 eV as predicted in this system should be clearly observable in experiments, manifesting as an energy difference between the optical absorption and emission peaks, a phenomenon known as the Stokes shift. A larger Stokes shift reduces overlap between absorption and emission spectra, which improves the signal-to-noise ratio in applications such as fluorescent dyes for biological imaging [48]. A larger Stokes shift is also desirable for applications in luminescent solar concentrators as it reduces the overlap between the absorption and emission peaks, thus reducing reabsorption loss and increasing efficiency [14, 15, 49, 50]. On the other hand, a Stokes shift reduces the power conversion efficiency in photovoltaic applications through loss in the open-circuit voltage, as the energy difference corresponding to the Stokes shift is dissipated as heat through phonon emission [51, 52]. Hence, a detailed understanding of the Stokes shift, the factors contributing to it, and how to control it is crucial for optimizing this material for potential applications, including light emission diode, solar cell, and solar concentrator applications.

One potential method for tuning the Stokes shifts is by tailoring the types and concentrations of defects in the system. In quantum dots, Stokes shifts have been attributed to the presence of defects, including vacancies and dopants. For example, the large Stokes shift in PbS colloidal quantum dots has been attributed to the presence of vacancies [51], while Cu(In)-doped CdS [53, 54] and Ag-doped CdTe [55] quantum dots have been reported to exhibit large tunable Stokes shifts. Our work suggests that vacancies can also generate large Stokes shifts in monolayer SnS, although further experimental validation is required. A recent DFT study predicted that vacancies in monolayer phosphorene may also be associated with Stokes shifts [39], albeit on the order of 0.3–0.4 eV compared to the shifts of up to more than 1 eV which we predict in SnS. In contrast, the S vacancy in MoS_2 has been reported to be associated with minimal Stokes shifts, likely due to the limited structural relaxations of its stiffer lattice [56, 57].

TABLE II. Comparison of the charge transition levels for the Sn and S vacancies in monolayer and layered bulk SnS. The CTL positions (in eV) are reported relative to the VBM in each case. For double charge transitions (e.g., +2/0 and 0/−2), only a single value is reported, spanning two columns. The values in parentheses indicate CTLs which fall outside the PBE bandgap but within the experimental bandgap following the "extended gap scheme" applied in Ref. [19]. Our results predict that the CTLs for the Sn and S vacancies in monolayer SnS are all deeper than the corresponding CTLs in the layered bulk SnS.

		V_{Sn}		V_S			
		0/−1	−1/−2	+2/+1	+1/0	0/−1	−1/−2
Monolayer SnS							
This work	PBE	+0.54		+0.21	+0.31	+1.39	+1.47
	SCAN+ rVV10	+0.62	+0.72	+0.29	+0.42	+1.57	+1.66
Bulk SnS							
Ref. [19]	PBE	+0.03	+0.13	+0.64		(+1.13)	(+1.17)
Ref. [18]	PBE+D3	N.A.	N.A.	+0.65		N.A.	N.A.

Comparing our predicted vacancy formation energies and thermodynamic CTLs in monolayer SnS with those reported in the literature for layered bulk SnS, we find that the vacancies in the monolayer have similar CTLs as those in the layered bulk, although they are deeper within the bandgap than the corresponding CTLs in the bulk. Table II compares the CTLs for the Sn and S vacancies in monolayer SnS computed in this work, with the corresponding CTLs reported by Malone *et al.* [19] and Kumagai *et al.* [18] for layered bulk SnS. For the Sn vacancy, we predict the $0/-1$ and $-1/-2$ CTLs to be about 0.5 – 0.75 eV above the VBM, while Malone *et al.* [19] predicted both CTLs in bulk to lie less than 0.2 eV above the VBM, and Kumagai *et al.* [18] predicted that the Sn vacancy is most stable in the −2 charge state across the entire bandgap (i.e., no CTLs within the bandgap). For the S vacancy, we predict the $+2/+1$ and $+1/0$ CTLs to be 0.25 – 0.4 eV above the VBM, whereas both Malone *et al.* and Kumagai *et al.* predict the +2/0 CTL to be around 0.65 eV above the VBM. Finally, we predict the S vacancy to have $0/-1$ and $-1/-2$ CTLs within 0.2 eV below the CBM, while the corresponding bulk CTLs were not predicted to fall within the PBE bandgap, although Malone *et al.* reported the $0/-1$ and $-1/-2$ bulk CTLs to fall just below the CBM when the bandgap was extended to match the experimental bandgap.

Our predictions that the acceptor states of the Sn vacancy and the donor states of the S vacancy are deeper in the monolayer than in the layered bulk are likely due to the increase in the electronic bandgap of the monolayer, and the additional dielectric screening in bulk which helps stabilize the defects in

their charged state and reduces their ionization energy. This suggests that unlike in its bulk counterpart, Sn vacancies in monolayer SnS are unlikely to be the source of *p*-type conductivity in the monolayer. A similar trend in the positions of the defect states has been predicted for S vacancies in monolayer and layered bulk MoS_2 [37]. Some differences in CTL positions may also arise due to uncertainties in the band edge positions for different exchange-correlation functionals.

V. CONCLUSION

Using first-principles density functional theory calculations, we perform a detailed study of the equilibrium defect structures, formation energies, charge transition levels, and electronic structures of Sn and S vacancies in monolayer SnS. Both vacancies are stable in multiple charge states, and we utilize the charge correction scheme of Freysoldt and Neugebauer to obtain accurate defect formation energies and charge transition levels under the appropriate electrostatic boundary conditions for charged 2D systems. We show that the easily-distorted orthorhombic SnS lattice undergoes different relaxations around each vacancy depending on its charge state, creating lower energy defect states that can be occupied by electrons. We predict that the significant atomic relaxations between the equilibrium defect structures in different charge states give rise to giant Stokes shifts of over 1 eV for optical transitions during which the defect structure does not have sufficient time to fully relax. This is in contrast to vacancies in the more commonly studied 2D transition metal dichalcogenides, which are not associated with large lattice distortions and, hence, are unlikely to exhibit such behavior. Large Stokes shifts have been observed in some organic molecules and quantum dots which have found applications in fluorescent dyes and luminescent solar concentrators. The realization of large Stokes shifts in monolayer SnS may open new opportunities for increased efficiency in applications such as light-emitting diodes, solar cells, and solar concentrators. We hope that this work serves as a motivation for further detailed computational and experimental studies of defects and dopants in monolayer SnS and other emerging 2D semiconductors to uncover unique phenomena which will be crucial to realize the potential of 2D materials in novel applications.

ACKNOWLEDGMENTS

This work was supported by the National Science Foundation through the 2DCC-MIP under award DMR-1539916 and by the awards DMR-1748464 and OAC-1740251. Computational resources were provided by the University of Florida Research Computing Center.

[1] J. Vidal, S. Lany, M. dAvezac, A. Zunger, A. Zakutayev, J. Francis, and J. Tate, Appl. Phys. Lett. **100**, 032104 (2012).
[2] R. Fei, W. Li, J. Li, and L. Yang, Appl. Phys. Lett. **107**, 173104 (2015).
[3] H. Khan, N. Mahmood, A. Zavabeti, A. Elbourne, M. A. Rahman, B. Y. Zhang, V. Krishnamurthi, P. Atkin, M. B. Ghasemian, J. Yang, G. Zheng, A. R. Ravindran, S. Walia, L. Wang, S. P. Russo, T. Daeneke, Y. Li, and K. Kalantar-Zadeh, Nat. Commun. **11**, 3449 (2020).
[4] M. Wu and X. C. Zeng, Nano Lett. **16**, 3236 (2016).
[5] N. Higashitarumizu, H. Kawamoto, C.-J. Lee, B.-H. Lin, F.-H. Chu, I. Yonemori, T. Nishimura, K. Wakabayashi, W.-H. Chang, and K. Nagashio, Nat. Commun. **11**, 2428 (2020).
[6] A. S. Rodin, L. C. Gomes, A. Carvalho, and A. H. Castro Neto, Phys. Rev. B **93**, 045431 (2016).
[7] A. Singh and R. G. Hennig, Appl. Phys. Lett. **105**, 042103 (2014).
[8] B. C. Revard, W. W. Tipton, A. Yesypenko, and R. G. Hennig, Phys. Rev. B **93**, 054117 (2016).
[9] H.-Y. Song and J.-T. Lü, Chem. Phys. Lett. **695**, 200 (2018).
[10] Z. Tian, C. Guo, M. Zhao, R. Li, and J. Xue, ACS Nano **11**, 2219 (2017).
[11] J. Xia, X.-Z. Li, X. Huang, N. Mao, D.-D. Zhu, L. Wang, H. Xu, and X.-M. Meng, Nanoscale **8**, 2063 (2016).
[12] H. Zhang, Y. Balaji, A. N. Mehta, M. Heyns, M. Caymax, I. Radu, W. Vandervorstbd, and A. Delabie, J. Mater. Chem. C **6**, 6172 (2018).
[13] A. S. Sarkar, A. Mushtaq, D. Kushavah, and S. K. Pal, npj 2D Mater Appl **4**, 1 (2020).
[14] F. Meinardi, H. McDaniel, F. Carulli, A. Colombo, K. A. Velizhanin, N. S. Makarov, R. Simonutti, V. I. Klimov, and S. Brovelli, Nat. Nanotechnol. **10**, 878 (2015).
[15] X. Hu, R. Kang, Y. Zhang, L. Deng, H. Zhong, B. Zou, and L.-J. Shi, Opt. Express **23**, A858 (2015).
[16] M. D. Smith, B. L. Watson, R. H. Dauskardt, and H. I. Karunadasa, Chem. Mater. **29**, 7083 (2017).
[17] C. Freysoldt, B. Grabowski, T. Hickel, J. Neugebauer, G. Kresse, A. Janotti, and C. G. Van de Walle, Rev. Mod. Phys. **86**, 253 (2014).
[18] Y. Kumagai, L. A. Burton, A. Walsh, and F. Oba, Phys. Rev. Appl. **6**, 014009 (2016).
[19] B. D. Malone, A. Gali, and E. Kaxiras, Phys. Chem. Chem. Phys. **16**, 26176 (2014).
[20] Z. Xiao, F.-Y. Ran, H. Hosono, and T. Kamiya, Appl. Phys. Lett. **106**, 152103 (2015).
[21] A. Shukla and N. K. Gaur, Physica E **120**, 114054 (2020).
[22] Y. Li, C. Xia, J. Du, W. Xiong, X. Lib, and S. Wei, Phys. Chem. Chem. Phys. **19**, 5423 (2017).
[23] H. Ullah, M. Noor-A-Alam, H. J. Kim, and Y.-H. Shin, J. Appl. Phys. **124**, 065102 (2018).
[24] F. Wang, L. Zhou, Z. Ma, M. He, F. Wu, and Y. Liu, Nanomaterials **8**, 789 (2018).
[25] G. Kresse and J. Furthmüller, Phys. Rev. B **54**, 11169 (1996).
[26] P. E. Blöchl, Phys. Rev. B **50**, 17953 (1994).
[27] G. Kresse and D. Joubert, Phys. Rev. B **59**, 1758 (1999).
[28] J. P. Perdew, K. Burke, and M. Ernzerhof, Phys. Rev. Lett. **77**, 3865 (1996).
[29] J. Sun, A. Ruzsinszky, and J. P. Perdew, Phys. Rev. Lett. **115**, 036402 (2015).
[30] J. Heyd, G. Scuseria, and M. Ernzerhof, J. Chem. Phys. **118**, 8207 (2003).

[31] J. Heyd, G. Scuseria, and M. Ernzerhof, J. Chem. Phys. **124**, 219906 (2006).
[32] H. Peng, Z.-H. Yang, J. P. Perdew, and J. Sun, Phys. Rev. X **6**, 041005 (2016).
[33] M. Methfessel and A. T. Paxton, Phys. Rev. B **40**, 3616 (1989).
[34] H. J. Monkhorst and J. D. Pack, Phys. Rev. B **13**, 5188 (1976).
[35] C. Freysoldt and J. Neugebauer, Phys. Rev. B **97**, 205425 (2018).
[36] C. Freysoldt, J. Neugebauer, A. M. Z. Tan, and R. G. Hennig, Phys. Rev. B **105**, 014103 (2022).
[37] A. M. Z. Tan, C. Freysoldt, and R. G. Hennig, Phys. Rev. Mater. **4**, 064004 (2020).
[38] A. M. Z. Tan, C. Freysoldt, and R. G. Hennig, Phys. Rev. Mater. **4**, 114002 (2020).
[39] B. Rijal, A. M. Z. Tan, C. Freysoldt, and R. G. Hennig, (2021), arXiv:2107.04849 [cond-mat.mtrl-sci].
[40] L. C. Gomes, A. Carvalho, and A. H. Castro Neto, Phys. Rev. B **94**, 054103 (2016).
[41] L. Huang, F. Wu, and J. Li, J. Chem. Phys. **144**, 114708 (2016).
[42] Y. Zhang, B. Shang, L. Li, and J. Lei, RSC Adv. **7**, 30327 (2017).
[43] B. R. Tuttle, S. M. Alhassan, and S. T. Pantelides, Phys. Rev. B **92**, 235405 (2015).
[44] C. Freysoldt, P. Eggert, P. Rinke, A. Schindlmayr, and M. Scheffler, Phys. Rev. B **77**, 235428 (2008).
[45] G. Davies and M. F. Hamer, Proc. R. Soc. Lond. A **348**, 285 (1976).
[46] A. Gali, E. Janzén, P. Deák, G. Kresse, and E. Kaxiras, Phys. Rev. Lett. **103**, 186404 (2009).
[47] T. A. Abtew, W. Gao, X. Gao, Y. Y. Sun, S. B. Zhang, and P. Zhang, Phys. Rev. Lett. **113**, 136401 (2014).
[48] Z. Gao, Y. Hao, M. Zheng, and Y. Chen, RSC Adv. **7**, 7604 (2017).
[49] C. Li, W. Chen, D. Wu, D. Quan, Z. Zhou, J. Hao, J. Qin, Y. Li, Z. He, and K. Wang, Sci. Rep. **5**, 17777 (2015).
[50] C. Yang, J. Zhang, W.-T. Peng, W. Sheng, D. Liu, P. S. Kuttipillai, M. Young, M. R. Donahue, B. G. Levine, B. Borhan, and R. R. Lunt, Sci. Rep. **8**, 16359 (2018).
[51] Y. Liu, D. Kim, O. P. Morris, D. Zhitomirsky, and J. C. Grossman, ACS Nano **12**, 2838 (2018).
[52] O. Voznyy, L. Levina, F. Fan, G. Walters, J. Z. Fan, A. Kiani, A. H. Ip, S. M. Thon, A. H. Proppe, M. Liu, and E. H. Sargent, Nano Lett. **17**, 7191 (2017).
[53] A. N. Yadav, A. K. Singh, D. Chauhan, P. R. Solanki, P. Kumar, and K. Singh, New J. Chem. **44**, 13529 (2020).
[54] M. Liu, W. Yao, C. Li, Z. Wu, and L. Li, RSC Adv. **5**, 628 (2015).
[55] S.-J. Ding, S. Liang, F. Nan, X.-L. Liu, J.-H. Wang, L. Zhou, X.-F. Yu, Z.-H. Hao, and Q.-Q. Wang, Nanoscale **7**, 1970 (2015).
[56] S. Gupta, S. N. Shirodkar, D. Kaplan, V. Swaminathan, and B. I. Yakobson, J. Phys.: Condens. Matter **30**, 095501 (2018).
[57] I. Niehues, P. Marauhn, T. Deilmann, D. Wigger, R. Schmidt, A. Arora, S. Michaelis de Vasconcellos, M. Rohlfing, and R. Bratschitsch, Nanoscale **12**, 20786 (2020).